# A self-powered implantable and bioresorbable electrostimulation device for biofeedback bone fracture healing

Guang Yao[a,b,c,1,2], Lei Kang[d,e,1], Cuicui Li[d,1], Sihong Chen[b], Qian Wang[b], Junzhe Yang[d], Yin Long[a,b], Jun Li[a], Kangning Zhao[a], Weina Xu[a], Weibo Cai[e,2], Yuan Lin[b,c,2], and Xudong Wang[a,2]

[a]Department of Materials Science and Engineering, University of Wisconsin–Madison, Madison, WI 53706; [b]School of Materials and Energy, State Key Laboratory of Electronic Thin Films and Integrated Devices, University of Electronic Science and Technology of China, Chengdu, Sichuan 610054, China; [c]School of Electronic Science and Engineering, the Center for Information in Medicine, University of Electronic Science and Technology of China, Chengdu, Sichuan 611731, China; [d]Department of Nuclear Medicine, Peking University First Hospital, Beijing 100034, China; and [e]Department of Radiology and Medical Physics, University of Wisconsin–Madison, Madison, WI 53705

Edited by David A. Weitz, Harvard University, Cambridge, MA, and approved June 1, 2021 (received for review January 13, 2021)

**Electrostimulation has been recognized as a promising nonpharmacological treatment in orthopedics to promote bone fracture healing. However, clinical applications have been largely limited by the complexity of equipment operation and stimulation implementation. Here, we present a self-powered implantable and bioresorbable bone fracture electrostimulation device, which consists of a triboelectric nanogenerator for electricity generation and a pair of dressing electrodes for applying electrostimulations directly toward the fracture. The device can be attached to irregular tissue surfaces and provide biphasic electric pulses in response to nearby body movements. We demonstrated the operation of this device on rats and achieved effective bone fracture healing in as short as 6 wk versus the controls for more than 10 wk to reach the same healing result. The optimized electrical field could activate relevant growth factors to regulate bone microenvironment for promoting bone formation and bone remodeling to accelerate bone regeneration and maturation, with statistically significant 27% and 83% improvement over the control groups in mineral density and flexural strength, respectively. This work provided an effective implantable fracture therapy device that is self-responsive, battery free, and requires no surgical removal after fulfilling the biomedical intervention.**

nanogenerator | biofeedback therapeutics | closed-loop electrostimulation | bone fracture healing | bioresorbable electronics

Bone fracture, a typical musculoskeletal disorder, represents a significant problem in public health (1–3). High force impact or stress greater than the bone bearing capacity can cause fractures, while minimal trauma injury can also lead to fragility fracture under certain pathologic conditions, such as osteoporosis and osteogenesis imperfect (4, 5). Millions of people have suffered from bone fractures, and around 6 million people each year broke a bone in the United States alone. Fracture incidence increased with age in both sexes, where around 9 million fractures (more than 2 million in the United States) were related to age-related bone fragility each year worldwide (1). The bone fragility associated with age is a result of lower-than-normal maximum bone mass and greater-than-normal bone loss, which increases the difficulty of self-healing after fracture and the risk of nonunion (6). In addition, age-adjusted rates were 49% greater among women due to the decrease in bone density occurring after the menopause (1, 7). Bone fractures also incur tremendous costs; for example, the costs of fragility fractures in 2005 for the United States was $16.91 billion and projected worldwide expenditure would rise to $131.5 billion for the year of 2050 (8, 9). Numerous drugs and treatments have been developed to achieve regeneration and reproduction of bone tissue, preventing fracture and promoting effective fracture healing. Nevertheless, common drugs such as vitamin D and calcium supplements have insignificant impacts (10), while pharmacological drugs (e.g., bisphosphonates, antibody romosozumab) or hormone therapy all have side effects and require long-term continuous treatment (11, 12). Stem cell therapy has now been showing a big impact to nonunion bone fracture, which is still in the preclinical stage and can be very costly (13, 14).

Electrostimulation (ES), simulating the endogenous electric fields to modulate the bioelectric state and accelerate fracture healing, comes to the fore as a promising nonpharmacological treatment in clinical practice and has been approved by the US Food and Drug Administration (15). Pulsing electric fields with appropriate strength and frequency can activate cell-related gene expression, promote the proliferation and differentiation of injured tissue cells, and actively stimulate tissue regeneration (16). However, clinically available electrical interventions rely on large and complex equipment, which require frequent clinic visits and professionally trained clinicians to operate. State-of-the-art clinical study demonstrated that by correlating the stimulation amplitude and frequency directly to dynamic locomotion, biofeedback ES therapy is particularly

## Significance

Bone fracture represents a significant problem in public health. State-of-the-art clinical study demonstrated that by correlating the stimulation amplitude and frequency directly to dynamic locomotion, biofeedback electrostimulation therapy is particularly effective compared to conventional continuous electrostimulation for postoperative therapy and rehabilitation after musculoskeletal injury. However, implementation of biofeedback still relies on complex electronics and sensing systems, which largely limits its accessibility to patients. Here we developed a self-powered implantable and bioresorbable device that directly applies biofeedback electrostimulations to the treatment of bone fracture. The electrostimulation signals are generated solely from relevant body motions, providing a closed-loop biofeedback therapy bringing rapid healing to fractures. This device is self-responsive, battery free, and requires no surgical removal after fulfilling the biomedical intervention.

Author contributions: G.Y., W.C., and X.W. designed research; G.Y., L.K., C.L., S.C., Q.W., J.Y., and K.Z. performed research; G.Y., C.L., Y. Long, J.L., W.X., W.C., and Y. Lin analyzed data; and G.Y., L.K., Y. Lin, and X.W. wrote the paper.

The authors declare no competing interest.

This article is a PNAS Direct Submission.



[1]G.Y., L.K., and C.L. contributed equally to this work.

[2]To whom correspondence may be addressed. Email: xudong.wang@wisc.edu, gyao@uestc.edu.cn, linyuan@uestc.edu.cn, or wcai@uwhealth.org.

This article contains supporting information online at https://www.pnas.org/lookup/suppl/doi:10.1073/pnas.2100772118/-/DCSupplemental.

Published July 6, 2021.

effective compared to conventional continuous ES for postoperative therapy and rehabilitation after musculoskeletal injury (17–19). To make this approach more accessible to patients with broken bones, implantable materials, such as bendable piezoelectric bone scaffolds, have been extensively investigated for fracture healing (14). Although these materials were found being able to promote cell proliferation and differentiation, their electric polarization came from the intrinsic material structures. Once screened, the electric potential would not be sensed further. Therefore, these materials were not able to actively provide pulsed ES as those received in regular clinical treatments (20, 21). Besides, these materials are not degradable and require additional surgery to remove, further limiting their practical application potential in fracture healing (22, 23). Recent studies revealed that the implantable nanogenerator (NG) could directly correlate biomedical ES to biomechanical motions and thus achieve self-powered and self-responsive ES with superb therapeutic results (24, 25). In vitro study also showed that ES from an NG could offer positive effects to promote osteoblast (OB) cell proliferation and differentiation (26). Herein, we present an implantable and ultraflexible bone fracture ES device (FED) completely made of biodegradable and bioresorbable soft and metallic materials. The triboelectric NG (TENG) component was configured with island-bridge electrodes and pyramidal microstructure arrays, offering excellent flexibility and appreciable electrical output. The FED was able to attach on irregular tissue surfaces and produce stable biphasic electric pulses in response to the movement of the knee joint. In vivo studies on rats showed a significantly accelerated bone fracture healing as short as 6 wk under FED treatment. Compared to control groups, the bone mineral density and flexural strength of the stimulation group were improved by 27% and 83%, respectively, which was comparable to the treatment results by clinical ES. Mechanism study revealed that the electric field generated by FED could simulate the secretion of multiple growth factors, facilitate OB

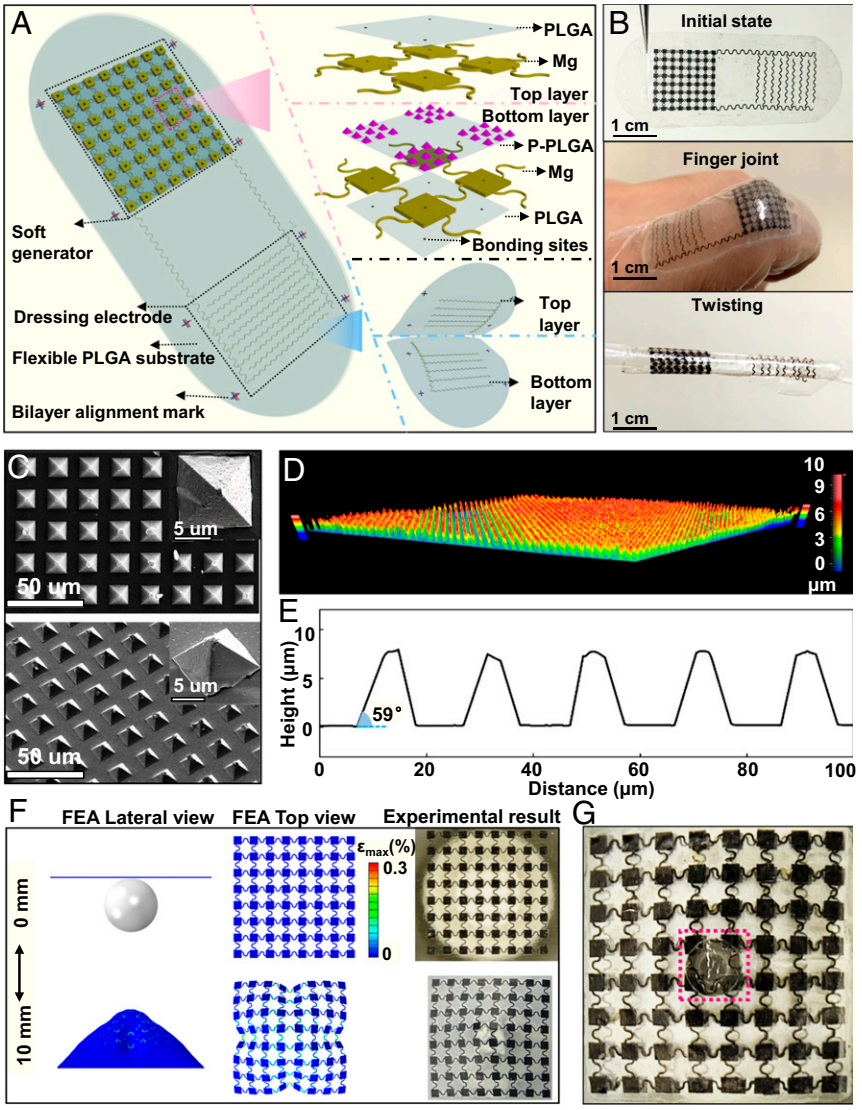


**Fig. 1.** Design and structural characterization of an FED. (*A*) Schematics of the overall FED structure (*Left*) and enlarged illustration of the device components, key materials, and multilayer structures (*Right*). (*B*) Optical image of an FED (*Top*) being fully bended at a finger joint (*Middle*) and being twisted (*Bottom*). (*C*) Top- and side-view scanning electron microscope images of the pyramid microstructures on the PLGA surface. *Insets* show enlarged views of a single pyramid. (*D*) Three-dimensional microscope photograph showing the uniform distribution of micropyramid arrays over a large PLGA surface. (*E*) Height profile along the top line of the PLGA micropyramids showing the good height uniformity. (*F*) FEA and experimental results of the island-bridge Mg electrode under different pressing height. (*G*) Optical image of water (pink dotted frame) droplet on the hydrophobic TENG with the pressing height of 10 mm.

proliferation, and thus promote bone formation, remodeling, maturation, and mineralization.

## Results and Discussion

**Design and Characterization of the FED.** As shown in Fig. 1*A*, the FED consisted of two modules: a TENG for electric pulse generation and a pair of interdigitated dressing electrodes providing a spatially distributed electric field. The detailed fabrication procedures of an FED are included in *SI Appendix*, Fig. S1. Both TENG and the dressing electrode components were built on the same piece of PLGA substrate. The TENG component had an island-bridge Mg bottom electrode, on top of which the micropyramid-structured PLGA (P-PLGA) layer was affixed with the pyramids pointing upwards. Together, they formed the bottom triboelectric layer. Another island-bridge Mg electrode-coated PLGA layer was capped and thermoplastically sealed on top of the P-PLGA layer, acting as the top triboelectric layer. The micropyramid structure of the P-PLGA could enhance the sensitivity and power generation density of the TENG due to improvement of the contacting interfaces (27, 28). A pair of interdigitated Mg dressing electrodes with a serpentine geometry was deposited 0.9 cm apart from the TENG component and connected via two serpentine lines. The overall dimensions of an FED were ~35 × 15 × 0.45 (L × W × T) $mm^3$. The island bridge and serpentine geometry can effectively promote the structure robustness, reduce the overall modulus, and minimize constraints on the flexibility of the FED. Therefore, the FED could be attached to irregular surfaces while subject to very large strains, such as on a fully bended finger joint or being twisted multiple turns (Fig. 1*B*).

The micropyramid structure on the PLGA surface was examined by scanning electron microscope, as shown by the top- and side-view images in Fig. 1*C*. All the micropyramids exhibited a uniform 10.5 × 10.5-$\mu m^2$ square base with a sharp pointing tip and were spaced 9.5 μm from each other. The large-scale uniformity of the micropyramid array was shown by a three-dimensional microscope scan of the P-PLGA film surface. It revealed that the height was ~8 μm with a small variation of ± 0.2 μm over a 0.85 × 0.85-$mm^2$ area (Fig. 1*D*). The cross-sectional height profile taken along one scanning line further quantified the geometry of the micropyramid array (Fig. 1*E*). The angle between the side and bottom surfaces was around 59°, confirming the perfect pyramid shape. The identical and uniform micropyramid structure is critical to achieve stable performance of the TENG (29, 30).

The mechanical robustness of the flexible island-bridge Mg electrode was first tested by a pressing system using a spherical plastic ball with a radius of 4 mm (*SI Appendix*, Fig. S2 *A*–*C*), where the length of Mg electrode islands ($L$) and their spacing in between were both designed as 800 μm. Finite element analysis (FEA) results of the Mg electrode under a series of tensile stresses consistently demonstrated that the strain was primarily distributed on the serpentine lines, and similar deformation behaviors were observed in FEA and experimental results (Fig. 1*F* and *SI Appendix*, Fig. S2 *D* and *E*). The strain (0.3%) subjected by the serpentine lines was consistently smaller than the failure strain (5%) even when the island-bridge Mg electrode film was pressed up to 10 mm, showing its excellent stretchability. In addition, the TENG encapsulated by the hydrophobic PLGA layer was also repeatedly pressed from 0 to 10 mm without any damage, which further confirmed the excellent mechanical robustness of the TENG component while maintaining a contact angle of 114.6° to act as a hydrophobic barrier from body fluids (Fig. 1*G* and *SI Appendix*, Figs. S2*F* and S3).

**Working Principle and Bioresorbable Behavior of the FED.** The electricity generation mechanism of the TENG followed the vertical contact-separation mode between the bottom P-PLGA and top Mg triboelectric layers (31, 32), and the corresponding motion cycle is depicted in Fig. 2*A*. The open-circuit peak-to-peak voltages between the top and bottom electrodes is defined as $V_{pp}$. At the initial stage, as the triboelectric layer is being separated, different electronegativity between bottom Mg and PLGA could induce positive and negative charges in Mg and PLGA, respectively (stage i). As the device was compressed, the micropyramids were deformed, yielding more contact area with the top Mg electrode. The closer contact depleted more electrons from the top Mg electrode and raised its electric potential (stage ii). As the deformation maximized (stage iii), the system reached a new equilibrium, where $V_{PP} = 0$. When the pressure was released, the pyramid structure started to recover its original shape and thus lowered the contact area with the top Mg electrode. Therefore, the electron depletion strength was reduced, and an electric field was built with $V_{PP} < 0$ (stage iv). When the top Mg electrode was fully released from the P-PLGA, a new balanced charge distribution could be built again ($V_{PP} = 0$). Owing to the high flexible and sharp micropyramid design, this contact-separation motion for electric pulse generation could be activated by many types of body movements, such as muscle stretching and knee bending. This allowed us to implant the FEDs near the fracture site providing ES to bone healing.

A mechanical linear motor was first employed to test the output performance of the TENG at low frequencies to simulate normal biomechanical motions. The FEDs made with different Mg island length $L$ (*SI Appendix*, Fig. S4) were tested at 1 Hz to reveal electrode design effect. As shown in Fig. 2*B*, $V_{PP}$ increased as $L$ increased from 200 to 600 μm and reached the maximum of 4.5 V when $L$ = 800 and 1,000 μm, then the $V_{PP}$ declined to 3.2 and 1.2 V as $L$ further increased to 2,000 and 4,000 μm, respectively. The decrease of $V_{PP}$ could be attributed to the limited area of ball pressing that might not activate all surface areas for charge collection at large $L$. Taking into account the output performance and flexibility together, the TENG with a Mg electrode size of $L$ = 800 μm was chosen for further animal studies. The output performance of this TENG was further characterized at a series of frequencies of 0.3, 0.5, 1.0, 2.0, 3.0, 4.0, and 5.0 Hz (Fig. 2*C*). $V_{pp}$ amplitudes increased monotonically from 0.5 to 6.8 V following the frequency increase, which could be attributed to the higher displacement rate leading to more rapid charge transfer. A lifetime test on an as-prepared FED was conducted for over 1,200 cycles (Fig. 2*D* and Movie S1). The nearly constant voltage output confirmed the good stability of ES generation over desired operation periods.

The FED was then implanted under the skin to test the in vivo voltage generation capability, with the TENG fixed at the site between the knee joint and the hip (Fig. 2*E*). The voltage output was monitored when the rat was at its normal activity (Fig. 2*F*, *SI Appendix*, Fig. S5 and Movie S2). It was found that the $V_{PP}$ during the rat's normal movements had a value of ~4 V, similar to the output induced by the mechanical actuator. This comparison confirmed that our FED could effectively convert random body motions into stable electric pulses. To evaluate the effectiveness of electric field penetration, Ansys Maxwell finite element solver (AMFES) was employed to estimate the electric field strength at the fracture site. AMFES simulation result showed that the interdigitated electrodes could generate a uniform electric field in its covered area (Fig. 2*G*). The electric field rapidly attenuated within the first 2 mm into the bone/tissue and slowly decayed to a low value of ~0.2 V/cm at 10-mm deep inside (Fig. 2*H*). The AMFES simulation suggested that the FED could implement stable and effective electric field stimulations into the bone when wrapped around the fractured area. In addition, since the thickness of insulating PLGA film was only ~200 μm, it would not induce any significant impacts to the electric field intensity applied to the fracture site.

The degradation and bioresorption behavior of FED was then studied in vitro and in vivo. First, the FED was immersed in a phosphate-buffered saline solution (pH 7.4) at 37 °C to investigate the degradation in vitro (Fig. 2*I*). The PLGA-encapsulated FED was relatively resistant to water uptake and mass loss during the first 12 wk. A remarkable mass loss and surface erosion took place

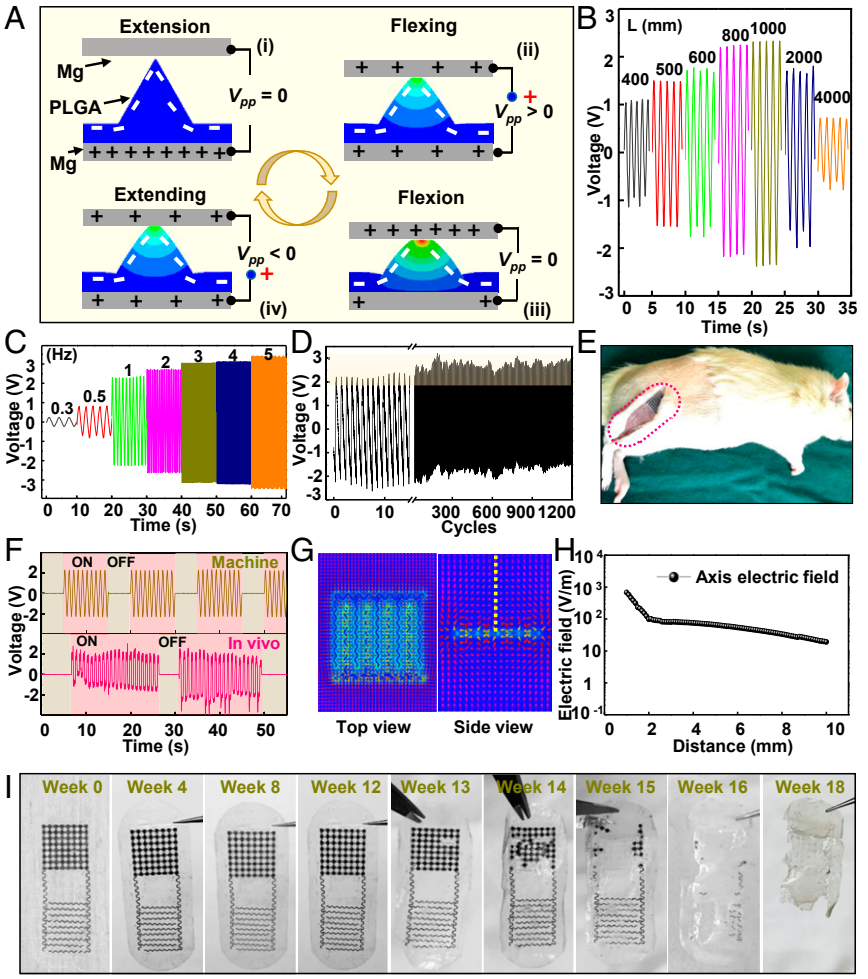


**Fig. 2.** Working principle, output performance, and degradation of FEDs. (*A*) Schematics of the working principle of the FED device under different knee joint motion stages. (*B*) Voltage output comparison of FEDs with different island length *L* at a frequency of 1 Hz. (*C*) Voltage output of FED with island length $L = 800$ μm at different frequencies. (*D*) Long-term stability test of TENG for over 1,200 cycles. (*E*) Optical image of an FED at the implanted site of an SD rat (pink dotted frame). (*F*) Voltage output recorded from the FED driven by a mechanical linear motor (*Top*) and on a rat in vivo (*Bottom*), respectively. (*G*) AMFES-simulated electrical field distribution inside a tissue ($V_{pp} = 4$V at an electrode gap width of 1 mm). (*H*) AMFES-simulated EF strength as a function of the depth into the tissue extrapolated from *G*. (*I*) Optical images of an FED in phosphate-buffered saline solution at 37 °C over 18 wk showing its natural degradation process.

at the 13th week when water infiltrated into the inner structure of the FED, followed by rapid autocatalytic hydrolysis and bulk degradation. The entire device disappeared after 18 wk. The in vivo biodegradation and resorption went through a similar process, where the FED appeared stable and unchanged during the first 8 wk and then degraded and resorbed quickly within 14 wk (*SI Appendix*, Fig. S6*A*). The in vivo degradation rate was relatively faster than in vitro, which might be related to the dynamic environment in the animal body. To reveal the stable functional period of the FED during implantation, voltage outputs were tested at different time points by harvesting the implanted FEDs from the rats (*SI Appendix*, Fig. S6 *B* and *C*). During the first 8 wk, the implanted FED showed a stable voltage output while the devices retained a good structural integrity in vivo. Compared to previous reports, our device exhibited a stable voltage output during a longer degradation time (33, 34). This could be attributed to the island-bridge configuration, thicker PLGA encapsulation, and the thermoplastic encapsulation strategy. Together, they could avoid the output attenuation caused by the encapsulation layer swelling, as well as eliminate bubbles or defects introduced during packaging. The 8 wk of stable function could provide sufficient ES intervention without the need of an invasive surgical removal process.

**Fracture Healing by FED Intervention and Mechanism Studies.** Before the intervention test, it is critical to ensure that the encapsulation material has an irritation-free contact with body tissue. Cytocompatibility of the FED was evaluated by comparing the morphology and proliferation of mouse fibroblast 3T3 cells cultured on an FED encapsulated by a PLGA layer and in a reference cultural dish for 3 d. Similar density and morphology were observed during 3 consecutive days of cell culture. Fluorescent staining images showed that the 3T3 cellular morphology spread from single cell to cell clusters on the encapsulation layer and the cultural dish (Fig. 3*A*). A 3-{4,5-dimethylthiazol-2-thiazolyl}-2,5-diphenyl-2H-tetrazolium bromide (MTT) assay was employed to characterize the viability of 3T3 cells in both groups (Fig. 3*B*). Compared to the normalized reference value in the culture dish, the relative viability on the PLGA layer was higher than 90% within 3 d and reached 96% on the third day. The normal spread and nonstagnation proliferation of 3T3 cells evidenced the nontoxicity and biocompatibility of the implanted FED.

The in vivo FED intervention study was focused on the right tibia of SD rats, which was fractured by three-point bending and stabilized by an intramedullary compression screw as reported previously (35, 36). This closed-fracture model was associated with

only minor soft tissue trauma and could provide a stable fixation of a standardized midshaft fracture of the tibia without affecting normal daily activity (Movie S3). The FED was implanted in the SD rats with working electrode wrapped around the fracture foci of the tibia and the TENG fixed at the site between the knee joint and the hip. The TENG harvested the knee joint motion energy to generate biphasic voltage pulses for fracture healing. The detailed fracture modeling and surgical procedures are shown in *SI Appendix*, Fig. S7. Whole-blood and chemical analysis were conducted on rats to evaluate the biosafety of FEDs during a 4-wk implantation period. The I group and Mg-implant group (M) were implanted by an FED and a piece of Mg film electrode, respectively (*SI Appendix*, Fig. S8*A*). The indicators of infection and immunity such as white blood cell (Fig. 3*C*), hematopoietic function such as red blood cell (Fig. 3*D*), and hemoglobin (*SI Appendix*, Fig. S8*B*), hepatological function such as alanine aminotransferase (Fig. 3*E*) and alkaline phosphatase (*SI Appendix*, Fig. S8*C*), and renal function such as creatinine (Fig. 3*F*) and blood urea nitrogen (*SI Appendix*, Fig. S8*D*) all remained steady during the entire implantation period. In general, all the blood testing results were within the normal range after the device implantation and did not show any abnormality (37, 38), suggesting that the FEDs and Mg electrodes are highly biocompatible and safe. In addition, the histological response of body tissue was investigated to evaluate the systemic influence of the implanted device. Skin at the fracture site of the tibia and tissues from important viscera including heart, liver, spleen, kidney, and lung were collected at 1, 2, 4, and 6 wk postimplantation for histological examination by hematoxylin-eosin (H&E) staining (Fig. 3*G*). H&E staining images of the I group and M group (*SI Appendix*, Fig. S8*E*) showed no signs of pathological inflammations or systemic immune responses such as abnormal lymphatic cells invasion in vital organs, excluding the risks of functional disorder and organic lesions. Therefore, the blood analyses and H&E results confirmed the good biosafety of the implanted FED, and there was no adverse local response during the ES intervention by the FED.

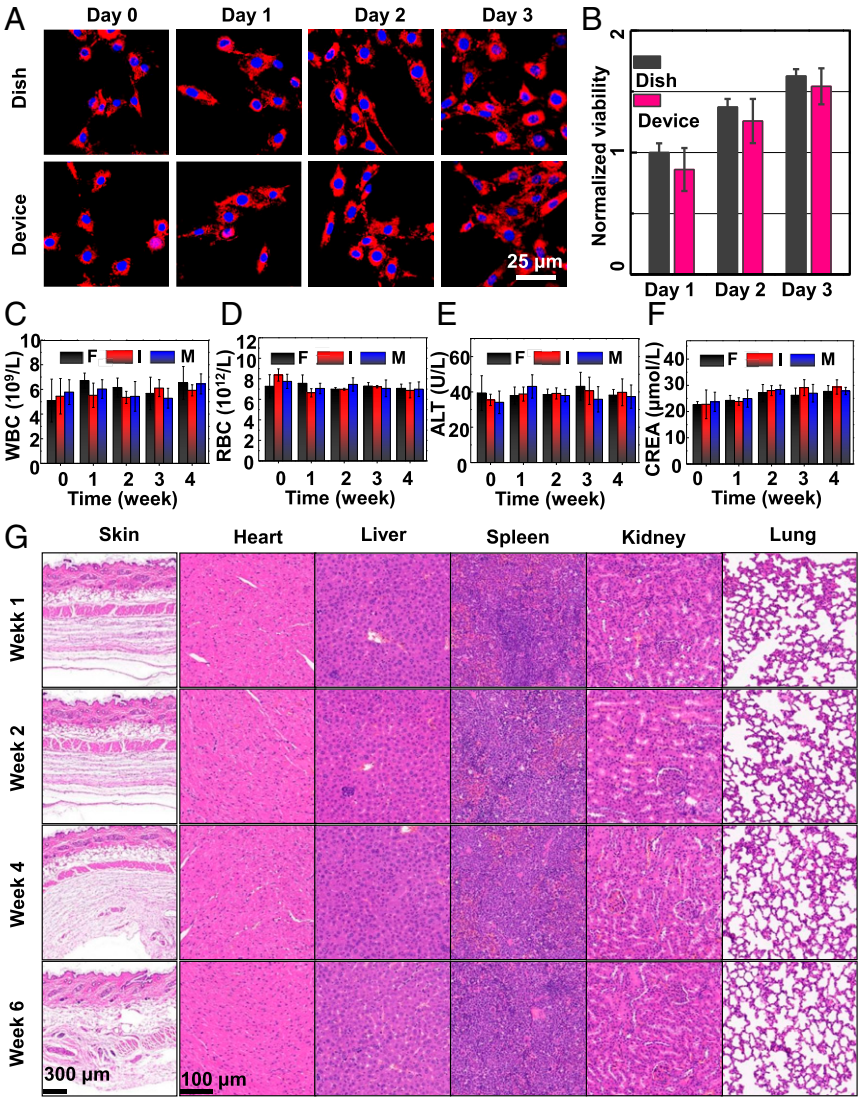


**Fig. 3.** Biocompatibility and long-term biosafety of the FEDs. (*A*) Fluorescence images of stained 3T3 cells that were cultured on a regular cell culture dish (*Top*) and on the surface of a PLGA-packaged FED (*Bottom*). (*B*) Comparison of normalized cell viability for 3 d showing excellent biocompatibility of the FEDs ($n = 3$ for each group). (*C*) Infection-related white blood cell (WBC) levels. (*D*) Hematopoietic function-related red blood cell (RBC) levels. (*E*) Hepatological function-related alanine aminotransferase (ALT) levels. (*F*) Renal function-related creatinine (CREA). (*G*) H&E stains of skin at the implantation site and vital organs (heart, liver, spleen, kidney, and lung) at different time points postimplantation. All data in *B* through *F* are presented as mean ± SD.

The bone fracture healing performance was then investigated in three groups of rats that were fed and grown under the same conditions. As schematically displayed in Fig. 4*A*, *Left*, the rats in intervention (I) group were stimulated by an implanted FED. Rats in sham (S) group were implanted with a deactivated FED device, where the dressing electrodes were disconnected from the TENG component. The false-implant (F) group had no implanted device. Both S and F groups were collectively referred as the control groups. All groups were subjected the same fracture surgery procedure. Clear fracture lines were observed in X-ray radiographs, indicating a closed-fracture model of right tibia was successfully created in all groups (Fig. 4*A*, *Middle*). After surgery, as well as before being euthanized, the rats were documented by X-ray scanning to monitor the fracture healing process. Enlarged X-ray radiographs at the fracture site from each group were recorded to analyze the intervention effect at different time points, and the rats were labeled as $I_n$, $S_n$, and $F_n$ ($n = 1, 2, 3, 4, 5, 6, 7$) (Fig. 4*A*, *Right* and *SI Appendix*, Fig. S9*A*).

Pathologically, the callus can be divided into the external callus produced by the periosteum and the internal callus produced by the fractured end and medullary cavity tissue during the process of fracture healing. The external callus close to the bone cortex at the broken front forms a short fusiform tube, which gradually merges to the fracture site and forms woven bone components through mineralization. Meanwhile, internal callus gradually transforms into cartilage tissue and then undergoes endochondral ossification to form cartilage internalized bone and dredge the marrow cavity. In the X-ray radiographs, the thickening of the fusiform short tube at the fracture and the blurring of the fracture line reflected the formation of external callus and internal callus, respectively. For group I, the fracture line started to blur at week 2, indicating internal and external callus gradually began to form. With the obvious increase of external callus, bridging callus was formed in the third week. The fracture line gradually disappeared, and the external callus maximized at week 4, which suggested the complete infiltration of new internal callus and the simultaneous dredging of the bone marrow. The bone remodeling phase started at week 5, marked by the gradual decrease of the external callus, which was gradually converted to normal compact bone from week 5 to week 6. Similar fracture healing processes were observed from both group S and F, indicating that the implantation of FED did not alter the natural fracture healing procedure.

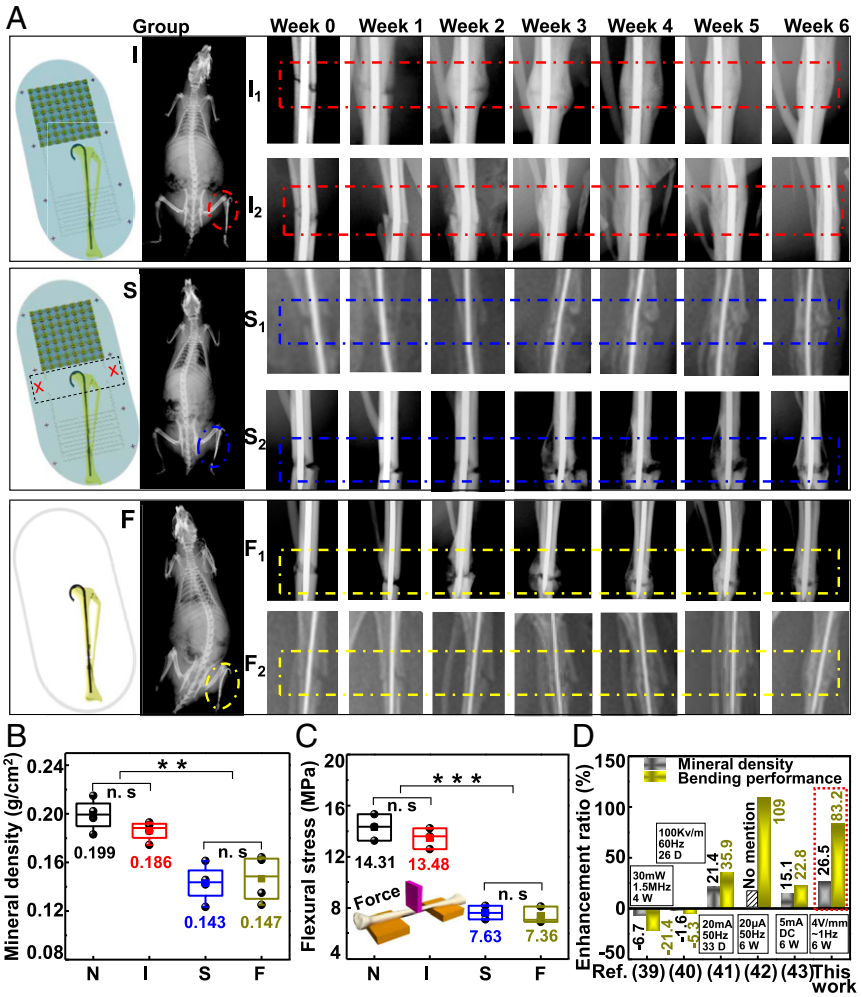


**Fig. 4.** Bone fracture healing analyses during FED intervention. (*A*) A series of X-ray radiographs on the bone fracture area over time of the Intervention group (I), sham group (S), and false-implant group (F) ($n = 7$). Schematics on the *Left* show the device setup of each group. (*B*) Mineral density of the fracture area from normal (N), I, S, and F groups after sacrifice in 6 wk ($n = 4$). (*C*) Three-point bending flexural stress measurement for different groups after sacrifice in 6 wk ($n = 4$). (*D*) Relative enhancement ratio of mineral density and bending performance in comparison to the reported results by electric intervention (pattern, frequency, and time were shown in the black wireframe, D represents days and W represents weeks). In box plots (*B* and *C*), dot is the mean, center line is the median, box limits are the lower quartile (Q1) and upper quartile (Q3), and whiskers are the most extreme data points that are no more than 1.5 × (Q3 − Q1) from the box limits. n.s, **, and *** represent nonsignificant ($P > 0.05$), $P < 0.01$, and $P < 0.001$, respectively.

In both control groups, the external callus began to form at week 3 and slowly evolved until week 6. However, the fracture line persisted, and bone marrow was not dredged throughout the entire 6-wk monitoring period. In addition, in the absence of electrical intervention, the fracture line did not completely disappear at week 10 and may even cause nonunion (*SI Appendix*, Fig. S9 *B* and *C*). It was obvious that the implanted FED significantly accelerated fractural healing by promoting bone callus formation and bone marrow dredging compared to the control (S and F) groups.

To further evaluate the healing results by FED intervention, the mineral density of the right tibia after 6 wk in I, S, and F groups was assessed and compared to a normal (N) group that did not receive any fracture surgery. The average mineral density of rats in N, I, S, and F groups is 0.199 and 0.186, 0.143, and 0.147 g/cm$^2$, respectively (Fig. 4*B* and *SI Appendix*, Fig. S10). No statistically significant mineral density was observed between groups I and N and between groups S and F. Group I also showed a statistically significant ($P < 0.05$) 27% improvement over both control groups in mineral density. The average flexural stresses of the tibia bone were measured from the N, I, S, and F groups by three-point bending to reveal their mechanical property (Fig. 4*C* and *SI Appendix*, Fig. S11). Similarly, statistically significant ($P < 0.001$) 83% improvement in group I (13.48 MPa) over the control groups (7.63 and 7.36 MPa for group S and F, respectively) was observed. Group I also did not show statistically significant difference compared to the normal group (14.31 MPa). Both results confirmed that FED intervention could rapidly bring the fractured bone to a healthy bone level in both bone mineral density and bone strength, significantly superior to the natural healing results. The fracture healing effect was further compared to other reported results by electrical intervention based on rat fracture models (Fig. 4*D*). The relative enhancement ratios of mineral density and bending performance were calculated from the difference between the intervention (I) and nonintervention fracture (F) groups. The comparison showed that our implanted FED intervention largely surpassed the performance of most previous ES methods (39–43).

To understand the accelerated fracture healing mechanism driven by FED intervention, multiple growth factors and cells related to bone growth were studied. Fracture healing is a unique cascade process that reinitiates morphogenetic processes of bone generation and mirrors the ontological events during embryological development of the skeleton. As shown in Fig. 5*A*, it typically occurs in four phases: 1) the hematoma formation and inflammatory phase, 2) callus generation, 3) primary bone formation, and 4) secondary bone remodeling (44, 45). In the bone fracture healing process, OB and osteoclast cells (OC) ensure normal bone metabolism and fracture healing through antagonistic synergy, accompanied by cell-related growth factors/cytokines regulation (*SI Appendix*, Fig. S12). Many growth factors/cytokines, expressed during fetal skeletal development and induced in response to injury, were believed to have a significant role in the process of fracture healing. These include members of the vascular endothelial growth factor (VEGF), fibroblast growth factor (FGF), transforming growth factor (TGF-β), as well as bone morphogenetic protein (BMP). At the end of week 6, bones in different groups were collected and measured by immunohistochemistry (IHC) and immunofluorescence to evaluate the distribution of these key growth factors to understand the FED intervention mechanism (Fig. 5 *B* and *C*). The growth factors, blood vessels, OB and OC were marked in 10× and 40× IHC staining images (Fig. 5*B*, *i* through *iv*, *SI Appendix*, Fig. S13). IHC staining images (10×) displayed an overall expression distribution of various growth factors and blood vessels (*SI Appendix*, Fig. S13). The cell types and growth factor expressions were marked in 40× IHC images, where dark brown color represented the expression of corresponding growth factors and cells were identified by colored circles based on their distinguishing morphologies. In general, the IHC results showed the secretion of VEGF, FGF1, TGF-β, and BMP2 in group I were significantly enhanced compared to the control groups (S and F groups), while there were no signs of any growth factor expression in group N. VEGF and FGF is a major mechanism by which angiogenesis and osteogenesis are tightly coupled, acting as metabolic supplier and well-characterized drivers during bone healing. Besides, more vascular vessels were found around the stronger expression area of VEGF and FGF1 in group I, indicating FED intervention could accelerate vascularization in fracture healing process (Fig. 5*B*, *i* and *ii*). The synergistic secretion enhancement of TGF-β and BMP2 could accelerate bone regeneration, and thus largely enhanced OB density was observed in group I, which could quickly start the bone remodeling phase, leading to a higher bone mineral density and a higher bone fracture strength (Fig. 5*B*, *iii* and *iv*). OC is another important sign of bone entering the remodeling phase along with the replacement of large fracture spongy callus by compact bone. The appearance of OC in group I further confirmed that the fracture healing reached the remodeling phase, while the control groups (S and F) were still in the primary bone formation stage without the present of OC (Fig. 5*B*, *ii*, *iii*, and *iv*).

Finally, receiver operating characteristic curve analysis was conducted to quantify the expression intensity of growth factors (46) (Fig. 5*D*). IHC scores were calculated by multiplying the percentage of stained cells (0 to 100%) by the intensity of the IHC staining (low, 1; medium, 2; and strong, 3). The average IHC scores of group I were 2.97, 2.98, 2.95, and 2.96 for VEGF, FGF1, TGF-β, and BMP2, respectively, which were statistically significantly higher than those of groups S (0.92, 0.88, 0.97, and 0.90) and F (0.90, 0.78, 0.83, and 0.88). Similarly, the immunofluorescence staining images (Fig. 5*C* and *SI Appendix*, Fig. S14) showed the secretion of VEGF (green), TGF-β (green), and BMP2 (red) in group I were significantly enhanced compared to the control groups (S and F groups), while there were no signs of any growth factor expression in group N. ImageJ software was used to quantify the expression levels of VEGF, TGF-β, and BMP based on their fluorescent intensities (Fig. 5*E*). The average fluorescent intensities of group I were 6.1E6, 6.5E6, and 6E6 for VEGF, TGF-β, and BMP2, respectively, which were statistically significantly higher than those of groups S (2.8E6, 2.6E6, and 2.8E6) and F (1.9E6, 1.7E6, and 1.8E6). It is worth noting that both the IHC scores from IHC staining and fluorescent intensities from immunofluorescence staining of the S group is slightly higher than those of the F group. This may be attributed to the slow degradation of bioactive Mg electrode from open gaps of the disconnected FEDs, where the presence of Mg ions could enhance expression of calcitonin gene related peptide and related growth factors. As the most important cell for fracture healing and bone regeneration, the number of active OB were counted from 40× IHC images (Fig. 5*F*). The average OB counts were 125, 121, 133, and 129 in VEGF, FGF1, TGF-β, and BMP2 staining images, respectively, which were about twice those of the group S (50, 50, 62, and 64) and group F (50, 62, 73, and 59). Meanwhile, there were no obvious signs of any OB in group N, which only had signs of osteocyte cells, representing the static period of bone growth. It should be noted that although individual growth factors have specific signal transduction mechanisms and associated receptors for realization of unique functions, fracture healing is a complex physiological process involving multiple cells and growth factors, and the bone tissue metabolism is cooperatively regulated and signaled by multiple factors.

## Conclusion

In this paper, we developed an effective fracture therapeutic strategy with an implanted flexible and bioresorbable FED. It could generate biphasic electric pulses in response to body movements, such as knee bending. The TENG component in FED had an island-bridge electrode and micropyramid structure, which rendered

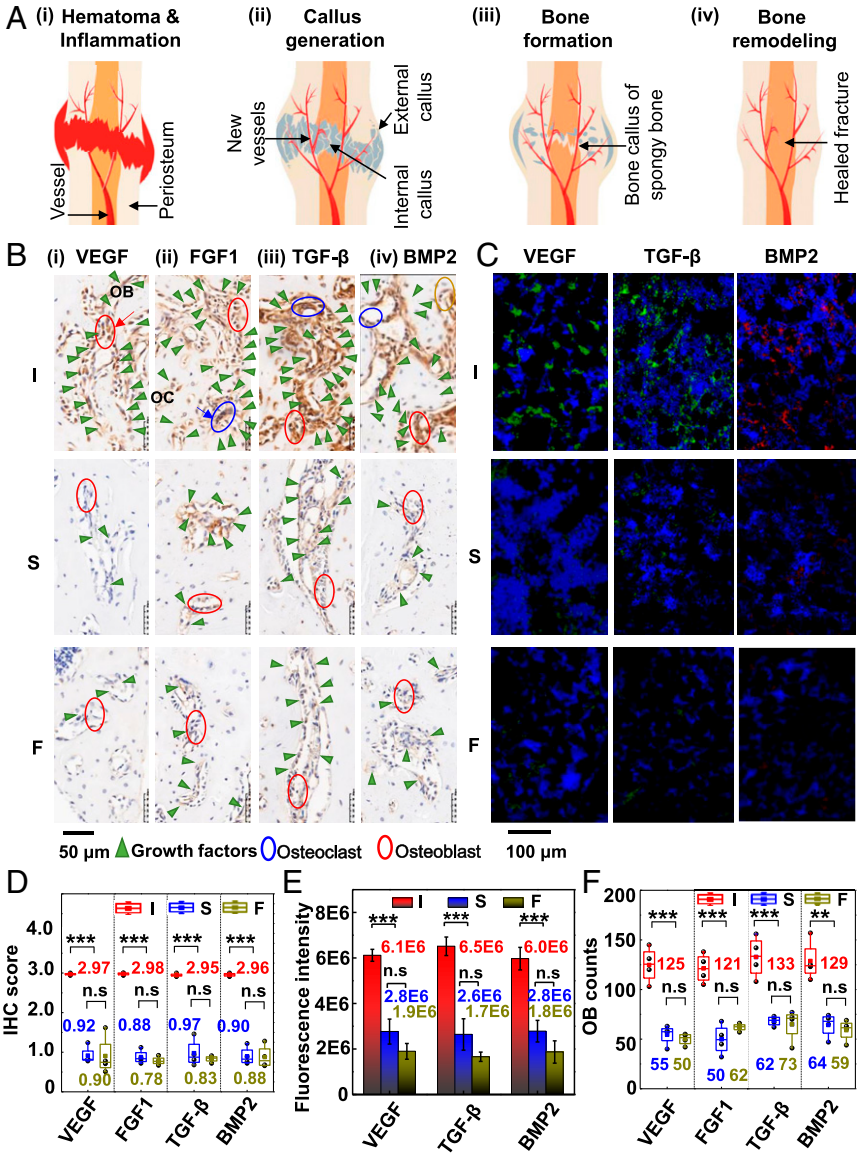


**Fig. 5.** Biological intervention mechanism of the FED. (*A*) Stages in fracture healing including a hematoma formation and inflammatory phase (i), callus generation (ii), primary bone formation (iii), and bone remodeling (iv). (*B*) IHC staining images (10× and 40×) of multiple growth factors including VEGF (i), FGF1 (ii), TGF-β (iii), and BMP2 (iv). (*C*) Immunofluorescence staining images of VEGF, TGF-β, and BMP2. (*D*) IHC score of the various growth factors expressed in different groups ($n = 4$). (*E*) Fluorescence intensity of growth factors expressed in different groups ($n = 3$). (*F*) Number of OB counted from 40× IHC staining images ($n = 4$). In box plots (*D* and *F*), dot is the mean, center line is the median, box limits are the lower quartile (Q1) and upper quartile (Q3), and whiskers are the most extreme data points that are no more than 1.5 × (Q3 − Q1) from the box limits. n.s, **, and *** represent nonsignificant ($P > 0.05$), $P < 0.01$, and $P < 0.001$, respectively.

a seamless and stable contact with irregular tissue surface for efficient biomechanical energy conversion. By optimizing the geometry of the Mg electrodes, the FED could provide 4.5 V voltage output based on contact-separation movements, which were sufficient to provide ES intervention to attached tissues to the depth of 10 mm. The entire FED was built based on biodegradable PLGA material. It showed excellent biocompatibility and biosafety to the biological system. When implanted at the fracture foci site of the tibia, the FED showed a stable electrical output of 4 V for over 6 wk. Afterward, the device could gradually degrade and be resorbed in the implantation environment without the requirement of invasive surgical removal. Through in vivo rat study, we confirmed that the FED intervention could largely accelerate the healing of tibia fractures. FED-dressed fractures exhibited a complete recovery in as short as 6 wk, with statistically significant 27% and 83% improvements over the nonintervention groups in mineral density and flexural strength, respectively. This outstanding fracture therapeutic effect surpassed most other reported ES methods. The enhanced secretion of VEGF and FGF1 could accelerated vascularization for nutritional supply and metabolic transportation, while more TGF-β and BMP2 led to cell differentiation, bone formation, and mineralization. Together, they promoted a rapid bone regrowth with synergistically raised bone mineral density and bone strength. The FED shown in this work represents a promising example of self-responsive closed-loop ES for biomedical applications. It holds great potential toward a convenient and effective ES therapeutic treatment for fracture healing, which may largely reduce the suffering of bone fracture patients.

## Materials and Methods

Details of fabrications and characterizations of the FED and the in vitro and in vivo experiments all appear in *SI Appendix*. All animal experiments were performed following the standard protocol approved by the University of Wisconsin Institutional Animal Care and Use Committee and the Institutional Animal Care and Use Committee in Peking University First Hospital (201822).

**Data Availability.** All study data are included in the article and/or supporting information.

**ACKNOWLEDGMENTS.** This work was supported by the National Institute of Biomedical Imaging and Bioengineering of the NIH under Awards R01EB021336 and P30CA014520. The content is solely the responsibility of the authors and does not necessarily represent the official views of the NIH. G.Y. and Y. Lin thank the National Natural Science Foundation of China under Grants 61825102 and 62001096, the Science and Technology Department of Sichuan Province under Grant 2021YJ0362, and the Fundamental Research Funds for the Central Universities, University of Electronic Science and Technology of China under Grant ZYGX2020ZB041.

1. S. Amin, S. J. Achenbach, E. J. Atkinson, S. Khosla, L. J. Melton, III, Trends in fracture incidence: A population-based study over 20 years. *J. Bone Miner. Res.* **29**, 581–589 (2014).
2. E. Yelin, S. Weinstein, T. King, The burden of musculoskeletal diseases in the United States. *Semin. Arthritis Rheum.* **46**, 259–260 (2016).
3. N. Harvey, E. Dennison, C. Cooper, Osteoporosis: Impact on health and economics. *Nat. Rev. Rheumatol.* **6**, 99–105 (2010).
4. I. R. Reid, A broader strategy for osteoporosis interventions. *Nat. Rev. Endocrinol.* **16**, 333–339 (2020).
5. F. Pouresmaeili, B. Kamalidehghan, M. Kamarehei, Y. M. Goh, A comprehensive overview on osteoporosis and its risk factors. *Ther. Clin. Risk Manag.* **14**, 2029–2049 (2018).
6. D. Holmes, Non-union bone fracture: A quicker fix. *Nature* **550**, S193 (2017).
7. A. Klibanski *et al*.; NIH Consensus Development Panel on Osteoporosis Prevention, Diagnosis, and Therapy, Osteoporosis prevention, diagnosis, and therapy. *JAMA* **285**, 785–795 (2001).
8. M. Ruiz-Adame, M. Correa, A systematic review of the indirect and social costs studies in fragility fractures. *Osteoporos. Int.* **31**, 1205–1216 (2020).
9. A. Odén, E. V. McCloskey, J. A. Kanis, N. C. Harvey, H. Johansson, Burden of high fracture probability worldwide: Secular increases 2010-2040. *Osteoporos. Int.* **26**, 2243–2248 (2015).
10. J. G. Zhao, X. T. Zeng, J. Wang, L. Liu, Association between calcium or vitamin D supplementation and fracture incidence in community-dwelling older adults: A systematic review and meta-analysis. *JAMA* **318**, 2466–2482 (2017).
11. M. K. Skjødt, M. Frost, B. Abrahamsen, Side effects of drugs for osteoporosis and metastatic bone disease. *Br. J. Clin. Pharmacol.* **85**, 1063–1071 (2019).
12. M. Lorentzon, Treating osteoporosis to prevent fractures: Current concepts and future developments. *J. Intern. Med.* **285**, 381–394 (2019).
13. E. P. McNeill *et al*., Characterization of a pluripotent stem cell-derived matrix with powerful osteoregenerative capabilities. *Nat. Commun.* **11**, 3025 (2020).
14. G. L. Koons, M. Diba, A. G. Mikos, Materials design for bone-tissue engineering. *Nat. Rev. Mater.* **5**, 584–603 (2020).
15. M. Griffin, A. Bayat, Electrical stimulation in bone healing: Critical analysis by evaluating levels of evidence. *Eplasty* **11**, e34 (2011).
16. J. M. Khalifeh *et al*., Electrical stimulation and bone healing: A review of current technology and clinical applications. *IEEE Rev. Biomed. Eng.* **11**, 217–232 (2018).
17. F. B. Wagner *et al*., Targeted neurotechnology restores walking in humans with spinal cord injury. *Nature* **563**, 65–71 (2018).
18. M. Capogrosso *et al*., A brain-spine interface alleviating gait deficits after spinal cord injury in primates. *Nature* **539**, 284–288 (2016).
19. L. Asboth *et al*., Cortico-reticulo-spinal circuit reorganization enables functional recovery after severe spinal cord contusion. *Nat. Neurosci.* **21**, 576–588 (2018).
20. B. Tandon, J. J. Blaker, S. H. Cartmell, Piezoelectric materials as stimulatory biomedical materials and scaffolds for bone repair. *Acta Biomater.* **73**, 1–20 (2018).
21. F. R. Baxter, C. R. Bowen, I. G. Turner, A. C. E. Dent, Electrically active bioceramics: A review of interfacial responses. *Ann. Biomed. Eng.* **38**, 2079–2092 (2010).
22. R. A. Perez *et al*., Therapeutically relevant aspects in bone repair and regeneration. *Mater. Today* **18**, 573–589 (2015).
23. H. Liu *et al*., Bioenergetic-active materials enhance tissue regeneration by modulating cellular metabolic state. *Sci. Adv.* **6**, eaay7608 (2020).
24. G. Yao *et al*., Self-activated electrical stimulation for effective hair regeneration *via* a wearable omnidirectional pulse generator. *ACS Nano* **13**, 12345–12356 (2019).
25. Y. Long *et al*., Effective wound healing enabled by discrete alternative electric fields from wearable nanogenerators. *ACS Nano* **12**, 12533–12540 (2018).
26. J. Tian *et al*., Self-powered implantable electrical stimulator for osteoblasts' proliferation and differentiation. *Nano Energy* **59**, 705–714 (2019).
27. J. H. Lee, R. Hinchet, S. K. Kim, S. Kim, S. W. Kim, Shape memory polymer-based self-healing triboelectric nanogenerator. *Energy Environ. Sci.* **8**, 3605–3613 (2015).
28. C. M. Boutry *et al*., Biodegradable and flexible arterial-pulse sensor for the wireless monitoring of blood flow. *Nat. Biomed. Eng.* **3**, 47–57 (2019).
29. F. R. Fan *et al*., Transparent triboelectric nanogenerators and self-powered pressure sensors based on micropatterned plastic films. *Nano Lett.* **12**, 3109–3114 (2012).
30. S. C. Mannsfeld *et al*., Highly sensitive flexible pressure sensors with microstructured rubber dielectric layers. *Nat. Mater.* **9**, 859–864 (2010).
31. H. Guo *et al*., A highly sensitive, self-powered triboelectric auditory sensor for social robotics and hearing aids. *Sci. Robot.* **3**, eaat2516 (2018).
32. Y. Ma *et al*., Self-powered, one-stop, and multifunctional implantable triboelectric active sensor for real-time biomedical monitoring. *Nano Lett.* **16**, 6042–6051 (2016).
33. J. Koo *et al*., Wireless bioresorbable electronic system enables sustained nonpharmacological neuroregenerative therapy. *Nat. Med.* **24**, 1830–1836 (2018).
34. Q. Zheng *et al*., Biodegradable triboelectric nanogenerator as a life-time designed implantable power source. *Sci. Adv.* **2**, e1501478 (2016).
35. V. Bradaschia-Correa *et al*., The selective serotonin reuptake inhibitor fluoxetine directly inhibits osteoblast differentiation and mineralization during fracture healing in mice. *J. Bone Miner. Res.* **32**, 821–833 (2017).
36. F. Bonnarens, T. A. Einhorn, Production of a standard closed fracture in laboratory animal bone. *J. Orthop. Res.* **2**, 97–101 (1984).
37. M. Giknis, C. Clifford, *Clinical Laboratory Parameters for Crl:CD(SD) Rats* (Charles River Laboratories, Wilmington, MA, 2006).
38. G. Yao *et al*., Effective weight control via an implanted self-powered vagus nerve stimulation device. *Nat. Commun.* **9**, 5349 (2018).
39. C. C. Medalha *et al*., Comparison of the effects of electrical field stimulation and low-level laser therapy on bone loss in spinal cord-injured rats. *Photomed. Laser Surg.* **28**, 669–674 (2010).
40. B. J. McClanahan, R. D. Phillips, The influence of electric field exposure on bone growth and fracture repair in rats. *Bioelectromagnetics* **4**, 11–19 (1983).
41. A. Zamarioli *et al*., Standing frame and electrical stimulation therapies partially preserve bone strength in a rodent model of acute spinal cord injury. *Am. J. Phys. Med. Rehabil.* **92**, 402–410 (2013).
42. M. Nakajima *et al*., Effect of electroacupuncture on the healing process of tibia fracture in a rat model: A randomised controlled trial. *Acupunct. Med.* **28**, 140–143 (2010).
43. Z. Wang, S. Hou, The research condition of application of electrical stimulation on fracture healing. *Chin. J. Med.* **40**, 51–53 (2005).
44. C. S. Bahney *et al*., Cellular biology of fracture healing. *J. Orthop. Res.* **37**, 35–50 (2019).
45. R. A. D. Carano, E. H. Filvaroff, Angiogenesis and bone repair. *Drug Discov. Today* **8**, 980–989 (2003).
46. K. Hajian-Tilaki, Receiver operating characteristic (ROC) curve analysis for medical diagnostic test evaluation. *Caspian J. Intern. Med.* **4**, 627–635 (2013).